Marine Geology 493 (2026) 107720

Contents lists available at ScienceDirect

Marine Geology

journal homepage: www.elsevier.com/locate/margo

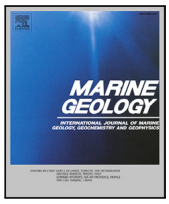

Research article

Effect of bed slope on turbidity currents interacting with an obstacle: Insights from Large Eddy Simulations

Said Alhaddad [a,*], Ching-Sen Wu [b], Lynyrd de Wit [c]

[a] Department of Maritime and Transport Technology, Faculty of Mechanical Engineering, Delft University of Technology, Leeghwaterstraat, Delft, 2628 CN, The Netherlands
[b] Department of Civil Engineering, National Ilan University, Yilan, 260007, Taiwan
[c] Deltares Delft, The Netherlands

ARTICLE INFO

Editor: Shu Gao

Code link: https://github.com/openearth/tudflow3d

Keywords:
Turbidity current
Triangular obstacle
Sediment deposition
Bed slope
Large Eddy Simulation

ABSTRACT

Understanding the behavior of turbidity currents is crucial for the effective and sustainable management of natural and artificial hydraulic systems. This study employs a high-resolution numerical model based on the Large Eddy Simulation (LES) approach to investigate the effect of bed slope on the dynamics and depositional behavior of turbidity currents interacting with a triangular obstacle in a channel. Six bed slopes were studied ranging from 0% to 4.5%. Our analysis focused mostly on the quasi-steady-state flow conditions upstream of the obstacle. The results reveal that steeper slopes enhance sediment transport capacity, leading to reduced sediment deposition rates along the bed and thus a decline in the obstacle's sediment-retention efficiency. The increased transport capacity primarily results from higher flow velocities rather than increased sediment concentrations. Detailed analysis of velocity distributions upstream of the obstacle, under quasi-steady state, showed that the velocity profiles are distorted differently among bed slopes as a result of the interplay between flow inertia and the adverse pressure gradient induced by the obstacle. Recirculation zones are observed for the milder bed slopes (0–1.5%), whereas these zones disappear for steeper slopes (3–4.5%), indicating the dominance of inertial effects.

1. Introduction

Turbidity currents are geophysical underwater flows that occur because of the density difference between a sediment-water mixture and the surrounding water. This difference generates a horizontal hydrostatic pressure gradient, driving the current downstream. These currents interact with the ambient fluid at the upper boundary and with the bed at the lower boundary, producing turbulence at both boundaries. Turbidity currents can be triggered through several natural and anthropogenic mechanisms, such as hypopycnal river plumes (Parsons et al., 2001), submarine slope failures (Alhaddad et al., 2020b, 2024a), dredging activities (Mahgoub et al., 2025), and deep sea mining (Alhaddad et al., 2024b). Therefore, gaining insight into the behavior and dynamics of turbidity currents is of great interest for both engineers and scientists.

In fact, turbidity currents are a fundamental sedimentary process in marine geology and represent the main mechanism by which sediment is transported from the continents into the deep sea, shaping deep-marine depositional systems (Talling et al., 2015; Kneller and Buckee, 2000). These flows are responsible for the formation of turbidite sequences that constitute a major component of the stratigraphic record in deep-water environments (Bourget et al., 2010). Additionally, turbidity currents are one of the primary mechanisms responsible for the transport and deposition of suspended sediments within reservoirs. These underflows can cause serious operational problems, such as clogging bottom outlets, obstructing hydropower intakes, and reducing the reservoir's storage capacity (Cesare et al., 2001; Oehy and Schleiss, 2007). To mitigate these effects, it is beneficial to control turbidity currents so that sediments settle in upstream areas before reaching critical structures near dams. Technical measures for managing turbidity currents are primarily designed to stop, dilute, or divert the flow, thereby reducing sediment deposition at sensitive locations. This can be achieved through the installation of engineered obstacles within the reservoir, such as submerged embankments (Oehy and Schleiss, 2007). Moreover, turbidity currents entering ocean basins interact with the seabed and its topographic irregularities, such as salt diapirs, seamounts, and volcanic islands. These features act as obstacles that impose resistance to the flow, leading to either partial or complete blockage (Cerqueira and Manica, 2022).

* Corresponding author.
E-mail address: S.M.S.Alhaddad@tudelft.nl (S. Alhaddad).

https://doi.org/10.1016/j.margeo.2026.107720
Received 1 December 2025; Received in revised form 29 January 2026; Accepted 1 February 2026
Available online 3 February 2026

Experimental studies examined how turbidity currents of varying densities and velocities interact with obstacles of different geometrical shapes and characteristics, including width and height (Alexander and Morris, 1994; Woods et al., 1998; Morris and Alexander, 2003; Abhari et al., 2018; Farizan et al., 2019; Cerqueira and Manica, 2022). Abhari et al. (2018) and Farizan et al. (2019) experimentally investigated the effect of obstacles on sediment transport in turbidity currents. The authors found that increasing the obstacle height leads to an increase in the suspended load transport rate upstream of the obstacle and a corresponding decrease downstream. The study conducted by Cerqueira and Manica (2022) showed that taller obstacles lead to greater blockage of the flow, causing a change in the flow regime from supercritical to subcritical. Numerous numerical studies have also been conducted to study the interaction between turbidity currents and an obstacle (e.g., Nasr-Azadani and Meiburg, 2014; Gonzalez-Juez et al., 2009; Goodarzi et al., 2020).

Reservoirs typically develop a sloping sediment bed—steep near the inflow and gradually flattening toward the dam. The influence of bed slope on the dynamics of unobstructed turbidity currents has been investigated in prior studies (e.g., Parker et al., 1987). Nevertheless, the effects of bed slope on the dynamics and depositional behavior of obstructed turbidity currents remain largely unexplored. This study addresses this gap by numerically examining these effects by simulating turbidity currents interacting with a triangular obstacle and propagating over different bed slopes ranging from 0% to 4.5%. This range is consistent with slopes used in experimental studies of reservoir turbidity currents (e.g., Chamoun et al., 2017). Detailed analyses of velocity and concentration distributions, along with layer-averaged parameters, are performed to elucidate the behavior of obstructed flows over varying bed slopes. This includes examination of the temporal development of the flow within the numerical domain as well as the spatial evolution of key turbidity current characteristics for the different slopes considered.

Various turbulence models and numerical approaches have been applied to investigate turbidity currents, including Direct Numerical Simulation (DNS) (Biegert et al., 2017), Large Eddy Simulation (LES) (Alhaddad et al., 2020a), and Reynolds-Averaged Navier–Stokes (RANS) equations (Choi and García, 2002). DNS resolves the full range of turbulent scales; however, applying it to turbidity currents interacting with obstacles would require very fine resolution near boundaries and interfaces, leading to substantially high computational cost. In contrast, LES models resolve the larger turbulent scales — which contain most of the turbulent kinetic energy — while filtering out the smaller eddies in a manner independent of specific flow conditions, since the governing equations are derived directly from the fundamental physical properties of turbulence. This approach allows LES to accurately represent the influence of density gradients on turbulence production and to capture the inherently anisotropic nature of turbulence at a much lower computational cost than DNS. Although RANS models are less computationally demanding than DNS and LES, they often fail to accurately capture regions of intense shear (e.g., near walls or obstacles) and flows characterized by low to moderate Reynolds numbers (Yeh et al., 2013). In this study, the LES approach is used as an effective balance between accuracy and computational cost.

The numerical model employed in the present study has been validated for a wide range of flow conditions relevant to the current work, including the front velocity of radially spreading turbidity currents flowing over both flat and sloping beds, sediment deposition from turbidity currents (de Wit, 2015), and velocity and concentration profiles of turbidity currents (Kirichek et al., 2021). Additionally, it has been successfully used for modeling the high-concentration breaching-generated turbidity currents (Alhaddad et al., 2020a).

The remainder of this paper is organized as follows. Section 2 provides background on the numerical model. Section 3 validates the model's performance against the experimental measurements of Abhari et al. (2018) and outlines the parameter space investigated. Section 4 presents and discusses the numerical results. Finally, Section 5 summarizes the key findings and conclusions of this study.

2. Numerical model description

Although LES has been applied in previous studies of turbidity currents, the combined effects of bed slope and flow obstruction remain unexplored. To address this gap, the LES framework is employed in conjunction with the mixture approach, enabling detailed analysis of flow structure and sediment transport over varying bed slopes. In this section, we briefly describe the used numerical model.

2.1. Governing equations

The flow of the turbidity current is mathematically described by the incompressible variable density Navier–Stokes equations. Using the mixture approach, the concentrations of the individual sediment fractions are solved separately while one set of momentum equations is solved for the water-sediment mixture (Manninen et al., 1996). Each sediment fraction has its own drift velocity $\boldsymbol{u}_d$, defined as the velocity of the sediment relative to the water-sediment mixture, which involves a correction of the mixture velocity with the equilibrium settling velocity of the sediment. The balance equations for the total mass and momentum of the mixture are stated as, respectively,

$$\frac{\partial \rho}{\partial t} + \nabla \cdot (\rho \boldsymbol{u}) = 0, \tag{1}$$

$$\frac{\partial (\rho \boldsymbol{u})}{\partial t} + \nabla \cdot (\rho \boldsymbol{u} \otimes \boldsymbol{u}) = -\nabla P + \nabla \cdot \boldsymbol{\tau} + (\rho - \rho_w)\boldsymbol{g}, \tag{2}$$

where t denotes time, ρ is the mixture density, ρ_w is the water density, $\boldsymbol{u}$ is the mixture velocity vector, P is the modified pressure, $\boldsymbol{\tau}$ is the shear stress tensor, $\boldsymbol{g}$ is the gravity vector, and ∇ denotes the spatial gradient operator. The shear stress tensor is proportional to the deviatoric strain rate of the mixture velocity,

$$\boldsymbol{\tau} = 2\mu \left(\nabla^s \boldsymbol{u} - \frac{1}{3} \nabla \cdot \boldsymbol{u} \right), \tag{3}$$

where μ is the dynamic viscosity of the mixture and $\nabla^s(\cdot) = \frac{1}{2}\nabla(\cdot) + \frac{1}{2}\nabla(\cdot)^T$ is the symmetric gradient operator. Although the model admits multiple sediment fractions (de Wit, 2015), a single sediment fraction is used in our study, meaning that the mixture density is given by,

$$\rho = \rho_w + (\rho_s - \rho_w)\, c_v, \tag{4}$$

where ρ_s is the sediment density, and c_v is the volumetric sediment concentration. The latter satisfies the following transport equation,

$$\frac{\partial c_v}{\partial t} + \nabla \cdot (\boldsymbol{u}_s c_v) = \nabla \cdot (\Gamma \nabla c_v), \tag{5}$$

in which $\boldsymbol{u}_s = \boldsymbol{u} + \boldsymbol{u}_d$ is the velocity of the sediment fraction, and Γ is the diffusivity which is related to the viscosity μ by,

$$\Gamma = \frac{\mu}{\rho_w Sc}, \tag{6}$$

where Sc is the Schmidt number ($Sc = 0.7$ is adopted in this study).

Obstacles within the computational domain are treated using a direct-forcing immersed boundary method (IBM) (Fadlun et al., 2000), which imposes zero velocity in cells located inside the obstacle. A first-order IBM representation is used, in which each computational cell is classified as either entirely fluid or entirely solid, with the latter assigned zero velocity.

2.2. Turbulence modeling

In our implementation, Eqs. (1), (2) and (5) are discretized using a regular rectangular grid with, possibly non-uniform, grid sizes (Δx, Δy, Δz in the respective Cartesian directions). Depending on the grid size, the finite resolution of the computed flow field can only partly include the relevant turbulence length scales. To account for the effect of the unresolved scales on the resolved flow field a turbulence closure model must be used.

In this study, Large Eddy Simulation (LES) is employed to explicitly resolve the turbulent flow dynamics. The LES approach applies a spatial filtering whereby turbulent fluctuations smaller than the grid size are parameterized through a sub-grid-scale (SGS) model, while energy-containing eddies larger than the filter width are directly resolved. By selecting a sufficiently fine grid resolution, the majority of the turbulent kinetic energy resides in the resolved scales, minimizing the contribution required from SGS modeling. Unlike the Reynolds-Averaged Navier–Stokes model that require empirical damping functions at sharp density interfaces, LES directly resolves the turbulent response to steep density gradients through the filtered momentum equations, allowing resolved turbulent structures to intrinsically respond to steep density gradients without requiring corrections. Furthermore, the non-isotropic behavior of the larger turbulent eddies is resolved in LES.

The eddy viscosity is modified to account for the influence of turbulence. To this end, the molecular viscosity μ_{mol} is enhanced with an extra sub-grid-scale viscosity μ_{sgs}, as follows,

$$\mu = \mu_{\text{mol}} + \mu_{\text{sgs}}, \tag{7}$$

where μ_{sgs} is a function of the strain rate tensor and the cell volume,

$$\mu_{\text{sgs}} = \rho \left(C_S \left(\Delta x \, \Delta y \, \Delta z\right)^{1/3}\right)^2 \|S\|, \tag{8}$$

in which C_S is Smagorinsky constant, and $\|S\|$ is some norm of the (filtered) velocity gradient tensor. For the latter, the WALE (wall adapting eddy viscosity) sub-grid-scale turbulence model (Nicoud and Ducros, 1999) is adopted together with a constant C_S of 0.325. This model can be considered a standard LES sub-grid-scale model, and is often used because it has the advantage of giving correct zero viscosity at solid walls without the need of wall-damping functions.

We use the wall-modeled LES approach, where a shear stress is applied at the wall as a partial slip boundary condition by calculating the local shear velocity vector $\boldsymbol{u}_*$ with a wall model. This approach gives accurate near-wall velocity profiles for sediment-laden turbulent flows and density currents (Kirichek et al., 2021; de Wit, 2015) and is accomplished by assuming a standard logarithmic velocity profile over the grid cell adjacent to the wall, which gives,

$$\boldsymbol{u}_* = \frac{\boldsymbol{u}_t}{\kappa^{-1} \ln\left(\frac{1}{2}\Delta Z / Z_0\right)}, \tag{9}$$

where $\boldsymbol{u}_t$ is the (filtered) tangential velocity vector in the grid cell adjacent to the wall, κ is the Von Kármán constant, ΔZ is the cell size normal to the wall, and $Z_0 = 0.11\nu/|\boldsymbol{u}_*| + k_n/30$, in which ν is the kinematic molecular viscosity of water, and k_n is the Nikuradse roughness height which is set to a value of $2\,d_{50}$ for the sediment bed and 0.2 mm for side-walls. Next, the wall shear stress, $\boldsymbol{\tau}_b$, is computed from,

$$\boldsymbol{\tau}_b = \rho \, |\boldsymbol{u}_*| \, \boldsymbol{u}_*. \tag{10}$$

The wall shear stress is applied as force term in the first computational cells next to a wall, a bed or obstacle. The wall model uses the instantaneous LES velocities to calculate the shear stress.

2.3. Numerical solution procedure

The spatial discretization of the model equations is based on a finite volume method, using a rectangular staggered grid in which the discrete velocity and pressure variables are located at alternating positions. The discretization in time conforms to a pressure-correction algorithm which involves a predictor step, in which an intermediate velocity field is computed using the pressure from the previous time step, followed by a corrector step, where the velocity and pressure are updated in a coupled fashion in order to satisfy the continuity constraint, Eq. (1).

In the predictor step an explicit third order Adams–Bashfort time integration scheme is employed, adjusted to be able to apply variable time step sizes. Small time steps are to be used with the Courant–Friedrichs–Lewy number (CFL-number) staying below 0.6. The IBM direct forcing step is carried out in the predictor step. The spatial discretization of the convection terms in the momentum equations is crucial for LES and is performed by a stable scheme with very low diffusion (de Wit and van Rhee, 2014). Likewise, the advection term in the transport equation is discretized with an accurate and robust TVD (Total Variation Diminishing) scheme employing the Van Leer limiter.

In the corrector step, the enforcement of the continuity constraint results in a pressure Poisson equation which is solved by a fast direct solver using the methodology of Dodd and Ferrante (2014). While for incompressible single-phase flows the continuity constraint implies zero divergence of the velocity field (by setting $D\rho/Dt = 0$ in Eq. (1)), this is generally not so for the flow of incompressible mixtures (Prosperetti and Tryggvason, 2007). This owes to the definition of the mixture velocity $\boldsymbol{u}$ in a densimetric manner, while zero divergence only holds for the *volumetric* mixture velocity. The latter is obtained by correcting the densimetric mixture velocity $\boldsymbol{u}$ with the respective equilibrium settling velocities from the sediment fractions - a necessary step preceding the enforcement of the zero divergence constraint. Overall, the numerical method is second-order accurate in time and space. For more details on the numerics, the reader is referred to de Wit (2015).

3. Model validation

As noted earlier, the numerical model employed in this study has been validated for a wide range of flow conditions relevant to the present work, including turbidity currents over sloping beds—validated in terms of front velocity, velocity and concentration profiles, and sediment deposition (de Wit, 2015; Alhaddad et al., 2020a; Kirichek et al., 2021).

To evaluate the applicability and reliability of the present numerical model for an obstructed turbidity current, a laboratory experiment carried out by Abhari et al. (2018) is reproduced numerically. In the validation case, a continuous dense current is introduced into the channel (L:11 m, W: 0.6 m, H: 0.6 m and bottom slope: 0.25%) and a triangle obstacle of 0.15 m height is located 4 m away from the inlet. The inlet geometry has a height of 0.04 m and a width of 0.06 m with its center coinciding with the center of the flume width. At the inlet, the initial sediment concentration C_0 is 5 kg/m^3, while the flow rate Q_0 is 0.25 l/s.

A rectangular computational domain is employed, aligned with the sloping bed. The gravity vector is rotated to ensure the correct gravitational influence on the turbidity current, with sediment settling occurring along this rotated direction. At the free surface, a rigid-lid, free-slip boundary condition is imposed. The domain width matches that of the experimental setup, and closed lateral boundaries are applied using a partial-slip condition with a wall roughness of k_n = 0.2 mm to represent wall-induced resistance on the current. A mesh-dependency study was conducted using four structured-grid resolutions (Mesh 1 - Mesh 4), where Mesh 1 is the coarsest and Mesh 4 the finest, along with a mean particle diameter of $D_{50} = 10\,\mu$m. The time-averaged velocity profiles at 2 m upstream of the obstacle were obtained at the quasi-steady state and compared with the experimental measurements.

Fig. 1 compares the velocity profiles from numerical simulations with the experimental measurements of Abhari et al. (2018). It can be seen that the numerical velocity structure is similar to the experimental one, with the velocities of the upper region somewhat smaller than the experimental ones. This is attributed to the fact that just one single particle diameter ($D_{50} = 10\,\mu$m) is used in the simulations and the finer particles are not represented. Goodarzi et al. (2020) showed that the velocity in the upper region of the turbidity current is increased when finer particles are introduced to the flow. In the physical experiments, Kaolin with a standard deviation $\sigma_g = \left(\frac{D_{84}}{D_{16}}\right)^{0.5} = 2.5$ was used, where D_{84} and D_{16} are particle diameters finer than 84% and 16% of particles, respectively. This means that the kaolin has a wide size distribution.

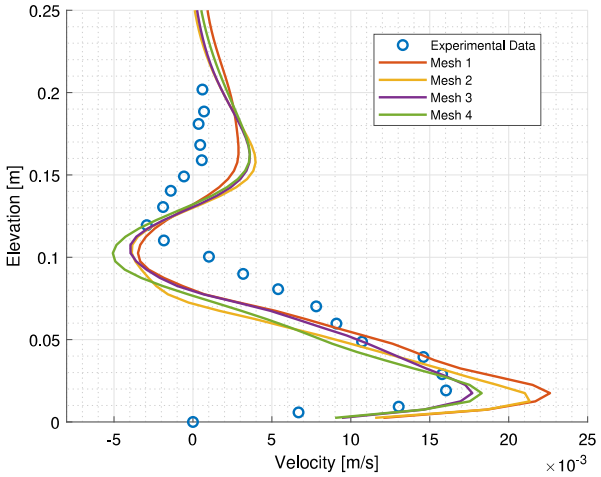

Fig. 1. Comparison of the numerical and physical modeling of the velocity profile at $x = 2$ m (2 m upstream of the obstacle).

Table 1
A summary of the numerical scenarios conducted in this study.

Simulation #	Inlet concentration [kg/m^3]	Inlet flow rate [l/s]	Bed slope [%]
1	5	0.25	0.00
2	5	0.25	0.25
3	5	0.25	1.00
4	5	0.25	1.50
5	5	0.25	3.00
6	5	0.25	4.50

While the solver used in this study can employ multiple particle sizes, the particle size distribution was not documented in Abhari et al. (2018). Consequently, a single sediment fraction ($D_{50} = 10\,\mu$m) has been used in the simulations.

The accuracy of the flow velocity in the lower region of the turbidity current is improved with mesh refinement, with negligible differences observed between Mesh 3 and Mesh 4. Considering the overall agreement across the full depth and the need for a computationally efficient framework for the subsequent parametric simulations, Mesh 3 was therefore chosen as the optimal compromise. To reduce computational time, grid clustering was applied in the x-direction (the stream-wise coordinate along the slope): the first 4.5 m of the domain used cells with a Δx of 10 mm, while the widths of the remaining cells gradually increased with a growth rate of 1.1, up to a set maximum of 5 cm. The cell dimensions in the y-direction (spanwise coordinate) and z-direction (bed-normal coordinate) were kept constant at 5 mm. The computational geometry used in the simulations is shown in Fig. 2, which illustrates the first 5 m of the numerical domain.

Six simulation scenarios are designed to determine the effect of the bed slope on the behavior of turbidity currents. The same numerical domain and conditions as those used in the validation case were applied, with the only exception being the variation in bed slope. A summary of these simulations is shown in Table 1.

4. Results and discussion

All simulations were run to 1860 s to ensure that a quasi-steady condition was achieved upstream of the obstacle, although this condition was reached at different simulation times depending on bed slope; in some cases, quasi-steady state was attained much earlier. The time-averaged quantities were obtained by temporally averaging the instantaneous values over the period 1800–1860 s, during which the flow was quasi-steady. In the following subsection, we discuss the evolution of the flow from its initial generation to the establishment of the quasi-steady state.

4.1. Flow evolution

To explore the temporal evolution of turbidity currents within the channel in the various cases considered, we plotted the dimensionless sediment concentration (c/C_0) fields from two perspectives—front view and top view at $z = 1$ cm above the sloping bed for three cases (0.25%, 1.5% and 4.5% bed slopes) in Figs. 3–5. These three slopes were selected as they capture the full range of flow behavior observed in all six simulated slopes. As expected, the front velocity of the flow increases with the bed slope. As the current propagates through the channel, the head of the current runs against the face of the obstacle and creates a backward-migrating turbidity bore, defined as a moving hydraulic jump. This jump changes the depositional pattern of the flow upstream of the obstacle (Yaghoubi et al., 2017). The other part of the current passes over the obstacle and moves forward. The horizontal velocity of the turbidity current decreases slightly as it ascends the obstacle, due to flow–obstacle interactions and the associated dissipation of turbulent kinetic energy. The bore gradually becomes thinner as it moves upstream. Analysis of the backward motion of the bores showed that the velocity of the bore decreases with an increased bed slope. For the milder bed slopes (0–1.5%), the bore propagates upstream and reaches the inlet boundary, indicating that the obstacle influences the sediment flux throughout the entire upstream region.

The right panels of Figs. 3–5 illustrate that the dimensionless sediment concentration upstream of the obstacle increases over time due to the partial obstruction of suspended sediment transport. Under quasi-steady conditions, the downstream concentration increases with increasing bed slope, indicating that the sediment-retention efficiency of the obstacle decreases as the bed slope becomes steeper, as will be discussed in details later in this study.

4.2. Upper boundary of turbidity currents

We plotted the interface between the turbidity current and the ambient water for all considered cases under quasi-steady conditions (Fig. 6). Notably, the interface upstream of the obstacle is nearly horizontal for all bed slopes. This is consistent with the observations of Abhari et al. (2018), where a similar behavior was reported for a bed slope of 0.25%. Our results further show that the interface orientation relative to the bed varies with bed slope under quasi-steady conditions. When the bed slope is zero, the interface remains parallel to the bed. As the slope increases, the interface gradually becomes oblique relative to the bed, reaching its steepest inclination at a 4.5% bed slope. It is also evident that the current thickness at the inlet is significantly reduced for the 3% and 4.5% cases while it rises toward the obstacle. It can be inferred from the interfaces that the bore stabilizes at quasi-steady state in all considered cases.

4.3. Velocity and concentration profiles

Fig. 7 presents the streamwise velocity and sediment concentration profiles for all simulated cases at a location $x = 1.5$ m under quasi-steady-state conditions. Overall, the velocity near the bed increases with increasing bed slope, whereas the sediment concentration decreases as the slope becomes steeper, indicating a reduction in the amount of suspended material within the current. This occurs because, at steeper slopes, a larger portion of sediment particles is able to pass over the obstacle, as illustrated in Figs. 3–5. This behavior suggests that, for steeper slopes, the driving mechanism of the flow becomes increasingly governed by the gravitational component associated with the bed inclination, next to the density contrast between the sediment-laden flow and the ambient fluid. Consequently, the enhanced downslope motion is primarily attributed to gravitational acceleration rather than density differences alone.

When a turbidity current approaches an obstacle, the flow decelerates and adjusts to the presence of a solid boundary, resulting in a

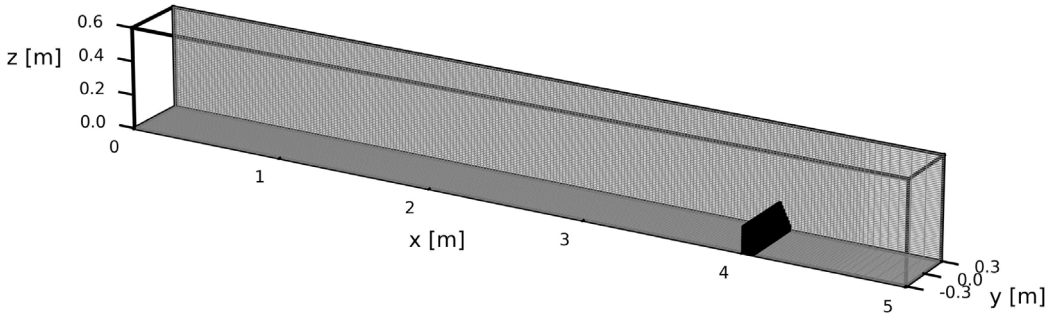

Fig. 2. Geometry used in all numerical simulations (first 5 m of the numerical domain); the current travels from left to right.

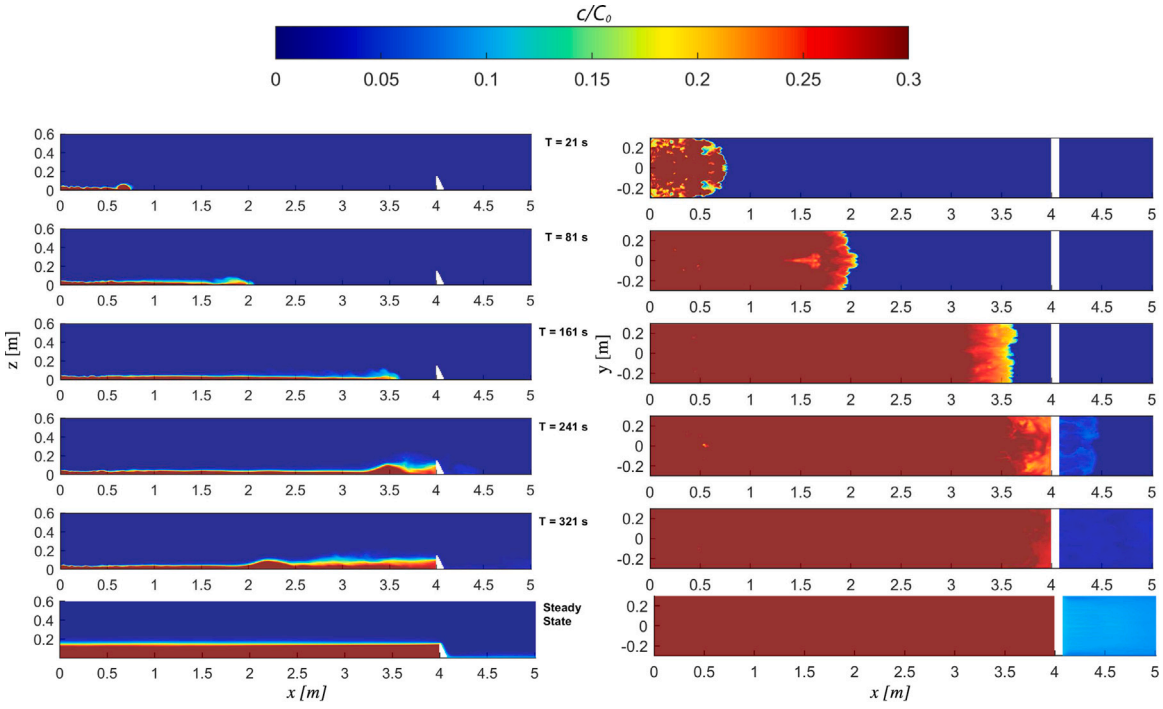

(a) *Front view (vertical central slice)* **(b)** *Top view (horizontal slice at z = 1 cm)*

Fig. 3. Temporal evolution of turbidity currents running over a 0.25% bed slope (21 s, 81 s, 161 s, 241 s, 321 s, and quasi-steady state). Colors represent the local dimensionless sediment concentration (c/C_0), where C_0 is the inlet sediment concentration.

complex redistribution of momentum and turbulence. Fig. 8 presents the streamwise velocity and sediment concentration profiles for all cases at a location 0.25 m upstream of the obstacle under quasi-steady-state conditions. In contrast to the profiles observed at $x = 1.5$ m, the velocity distributions exhibit two distinct positive peaks. The first peak occurs near the bed, consistent with the characteristic structure of unimpeded turbidity current velocity profiles, while the second peak develops near the crest of the obstacle. The approaching current accelerates locally over the obstacle's upstream face due to flow constriction, producing this secondary velocity maximum. A pronounced trough is evident between the two peaks, indicating flow recirculation or a localized reduction in streamwise velocity; this reduction is smallest for the steepest slopes (3% and 4.5%). The negative troughs in Cases 1–4 (0%–1.5% bed slopes) indicate the presence of a recirculation region, signifying backward motion of the current (see e.g., Figs. 9(a) and 9(b)). This recirculation arises from the adverse pressure gradient, as the pressure increases in the upstream direction due to the resistance imposed by the obstacle—opposing the flow motion. In contrast, no recirculation is observed in Cases 5–6 (3% & 4.5% bed slopes), where the flow inertia dominates over the adverse pressure gradient, allowing the current to maintain forward motion (see Figs. 9(c) and Fig. 9d).

The observed distorted velocity profiles are thus a manifestation of flow–obstacle interaction, resulting from the interplay between inertia and the adverse pressure gradient. As for concentration values, the same trend is observed as at $x = 1.5$ m; concentration values decrease with increasing bed slope.

Fig. 10 presents the streamwise velocity and sediment concentration profiles at the crest of the obstacle under quasi-steady-state conditions. The overall structure of the profiles is consistent with the experimental observations reported by Yaghoubi et al. (2017). In general, the velocity near the obstacle crest and within the upper region of the current increases with increasing bed slope. Although the concentration immediately above the obstacle crest does not increase with increasing bed slope, the concentration in the upper region of the flow correlates positively with bed slope. The flow also becomes thicker for steeper slopes, resulting in a greater overall amount of suspended sediment as the bed slope rises.

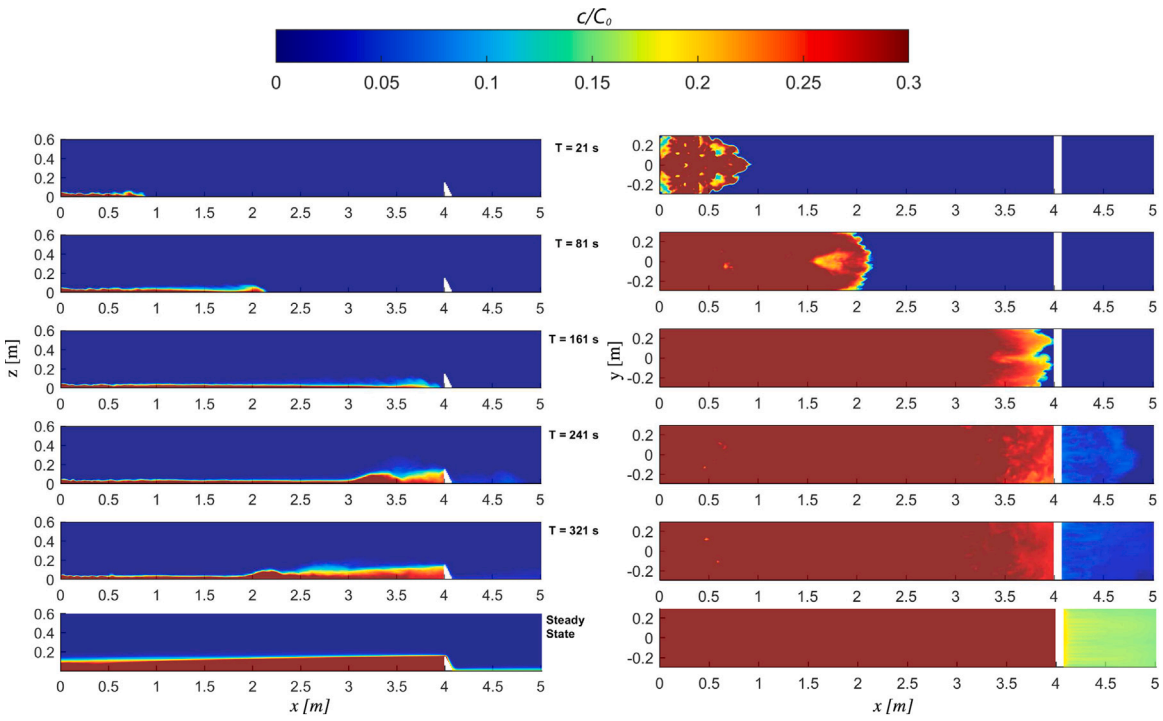

(a) *Front view (vertical central slice)* **(b)** *Top view (horizontal slice at z = 1 cm)*

Fig. 4. Temporal evolution of turbidity currents running over a 1.5% bed slope (21 s, 81 s, 161 s, 241 s, 321 s, and quasi-steady state). Colors represent the local dimensionless sediment concentration (c/C_0).

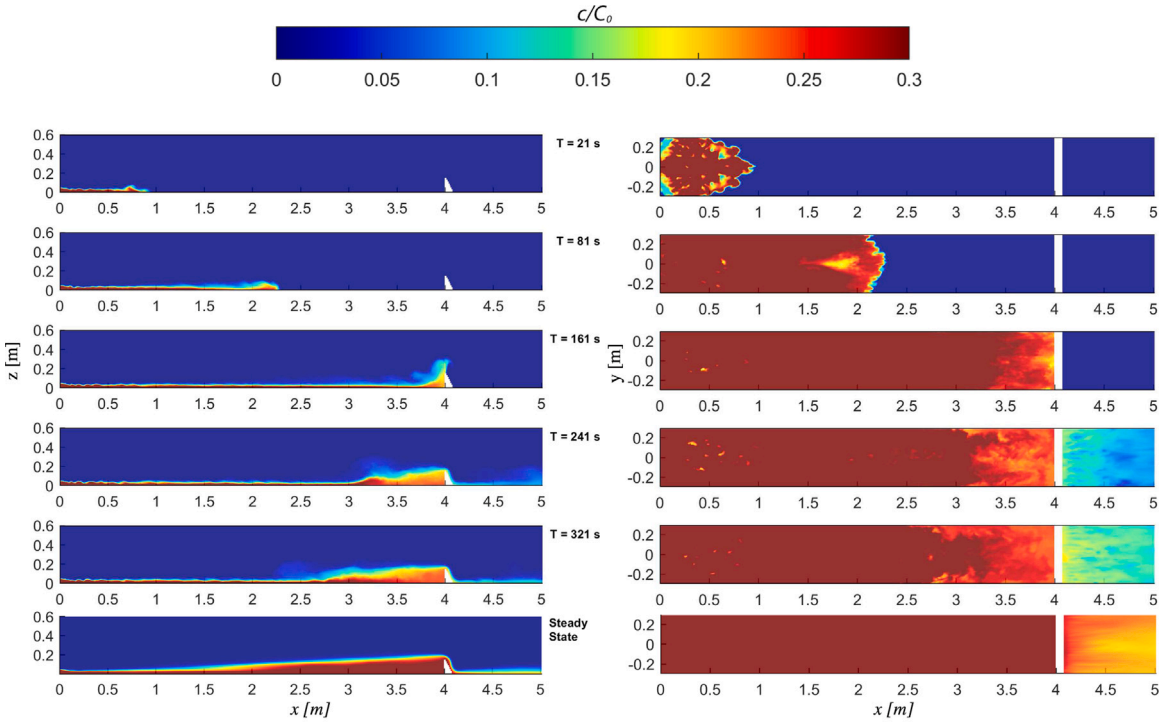

(a) *Front view (vertical central slice)* **(b)** *Top view (horizontal slice at z = 1 cm)*

Fig. 5. Temporal evolution of turbidity currents running over a 4.5% bed slope (21 s, 81 s, 161 s, 241 s, 321 s, and quasi-steady state). Colors represent the local dimensionless sediment concentration (c/C_0).

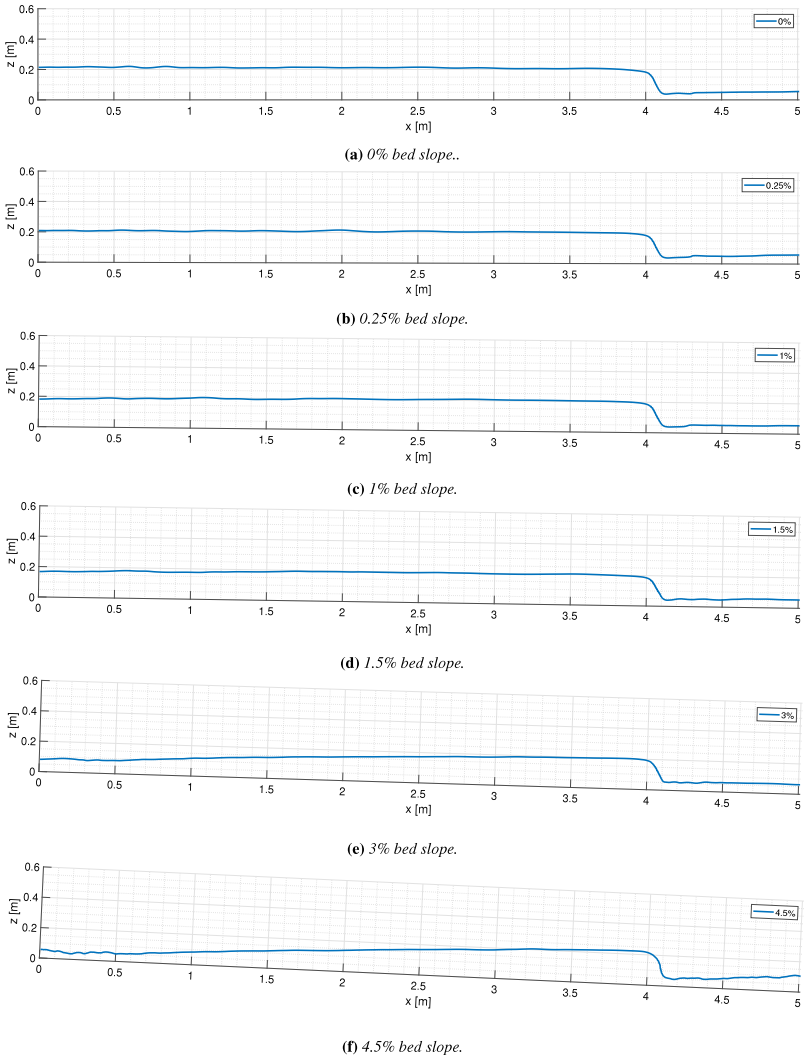

(a) *0% bed slope..*

(b) *0.25% bed slope.*

(c) *1% bed slope.*

(d) *1.5% bed slope.*

(e) *3% bed slope.*

(f) *4.5% bed slope.*

Fig. 6. Contours of the dimensionless concentration at 0.01 at the quasi-steady state.

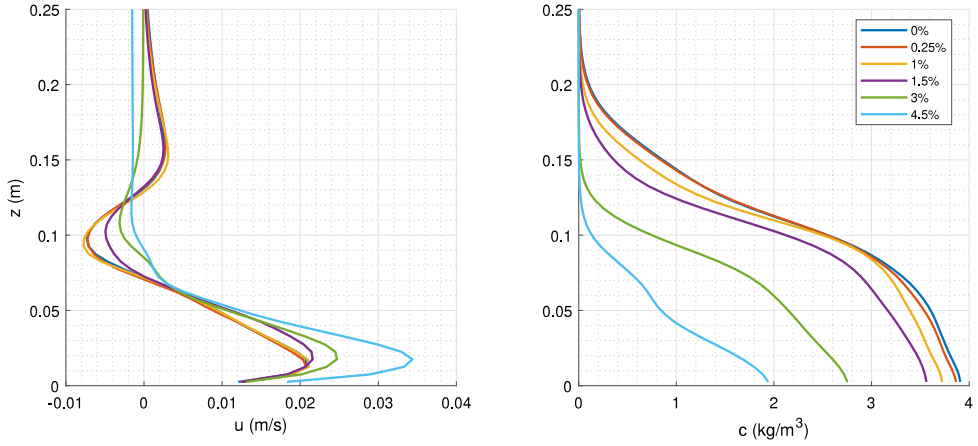

Fig. 7. Velocity and concentration profiles at $x = 1.5$ m for the various cases at the quasi-steady state.

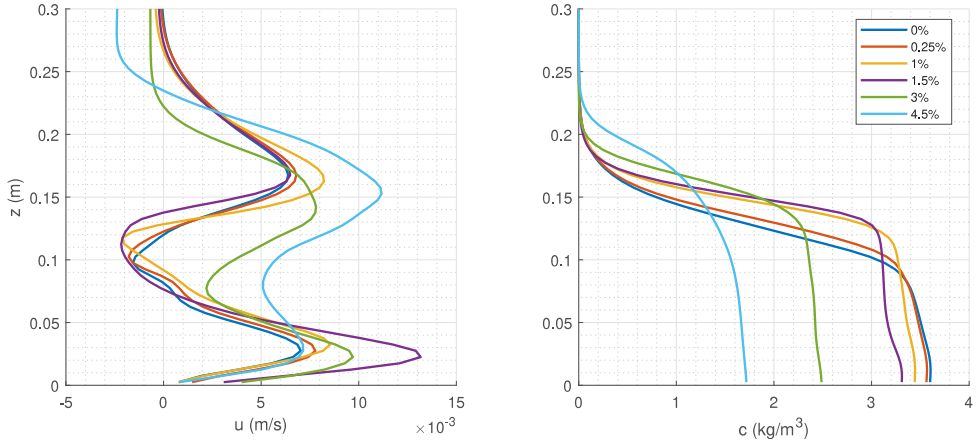

Fig. 8. Velocity and concentration profiles at $x = 3.75$ m (0.25 m upstream of obstacle) for the various cases at the quasi-steady state.

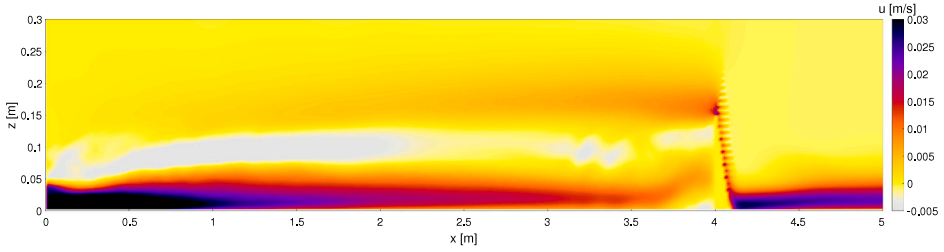

(a) *Turbidity currents running over a 1% bed slope*

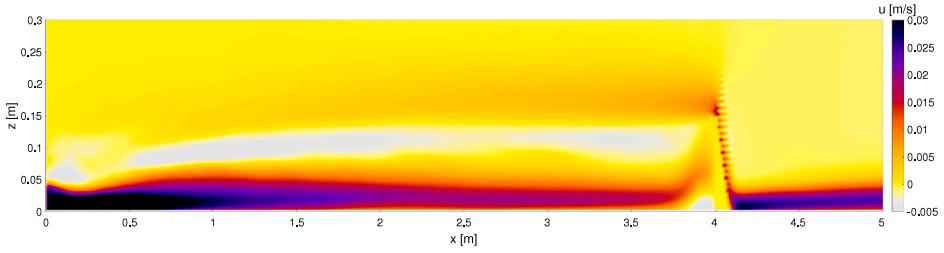

(b) *Turbidity currents running over a 1.5% bed slope*

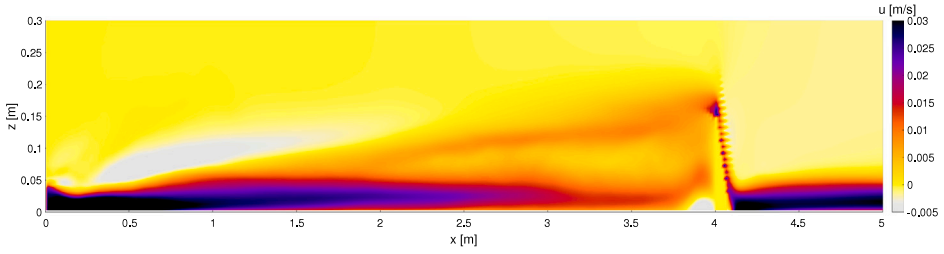

(c) *Turbidity currents running over a 3% bed slope*

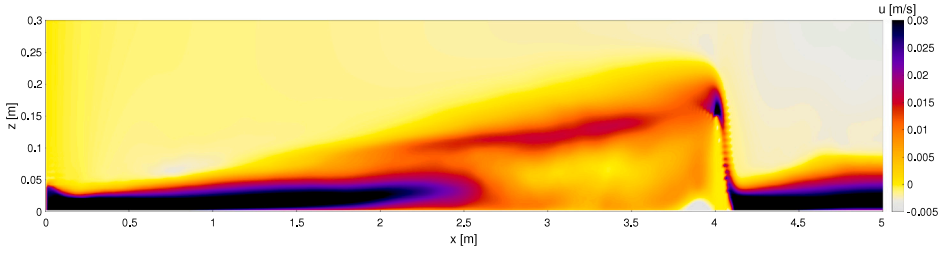

(d) *Turbidity currents running over a 4.5% bed slope*

Fig. 9. Streamwise velocity field of turbidity currents at the quasi-steady state; colors indicate the magnitude of streamwise velocity.

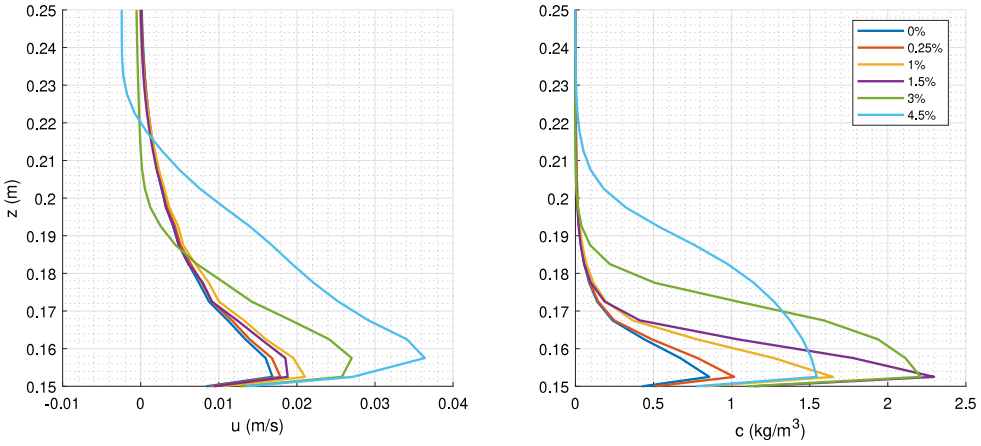

Fig. 10. Velocity and concentration profiles at $x = 4$ m (on top of obstacle) for the various cases at the quasi-steady state.

4.4. Streamwise evolution of layer-averaged characteristics

Using the streamwise velocity and concentration profiles, flow characteristics including the characterizing layer thickness h, the layer-averaged velocity U and the layer-averaged sediment concentration C are calculated using the following relationships:

$$Uh = \int_0^{z_\infty} u\,dz, \tag{11}$$

$$U^2 h = \int_0^{z_\infty} u^2\,dz, \tag{12}$$

$$C = \frac{\int_0^{z_\infty} cu\,dz}{\int_0^{z_\infty} u\,dz}, \tag{13}$$

where u is locally averaged streamwise flow velocity, c is local concentration of suspended sediment, z is upward-normal distance from the bed and z_∞ is the height at which the local velocity u is zero.

The spatial evolution of turbidity current characteristics for the considered cases is presented in Fig. 11. The layer-averaged streamwise velocity U decreases along the slope, reaching its minimum right upstream of the obstacle. A marked increase in U is observed immediately downstream of the obstacle. Overall, the layer-averaged streamwise velocity U increases with increasing bed slope, a trend that becomes more pronounced downstream of the obstacle. In contrast, the layer-averaged sediment concentration C exhibits lower values for steeper slopes upstream of the obstacle; however, this trend reverses in the downstream region, where higher C values are observed for steeper slopes. Once again, this indicates that at steeper slopes, a larger portion of sediment particles is able to pass over the obstacle.

4.5. Local densimetric Froude number

Here, we study the flow behavior using the local densimetric Froude number (the ratio of inertial forces to the reduced gravitational forces), which is calculated using the following relationship:

$$Fr_d = \frac{U}{\sqrt{\Delta g C_v h \cos\theta}}, \tag{14}$$

where $\Delta = \frac{\rho_s - \rho_w}{\rho_w}$ is the relative submerged density of sediment, C_v is the layer-averaged volumetric sediment concentration, and θ is the bed slope in degree.

Typically, flows with $F_{rd} > 1$ are considered supercritical whereas flows with $F_{rd} < 1$ are subcritical, though the value of the critical densimetric Froude number (F_{rd}), may be different in density currents (Huang et al., 2009; Dorrell et al., 2016). At the quasi-stead state, for bed slopes ranging from 0 to 1.5%, Fr_d decreases sharply near the inlet reaching unity between $x = 0.8$ and 0.94 m, whereas for the steeper slopes of 3% and 4.5%, the unity is reached further downstream at $x = 1.5$ m and $x = 2$ m, respectively (see Fig. 12). This indicates that $F_{rd} = 1$ is approached closer to the obstacle for the steeper slopes. In all cases, $Fr_d = 1$ is observed immediately downstream of the obstacle at $x = 4$ m. The local densimetric Froude number increases considerably after the current flows over the obstacle, changing the flow regime from subcritical to supercritical, with this increase being more pronounced at larger bed slopes. This increase in F_{rd} is a result of the rapid increase in the mean velocity of the current downstream of the obstacle (see Fig. 11).

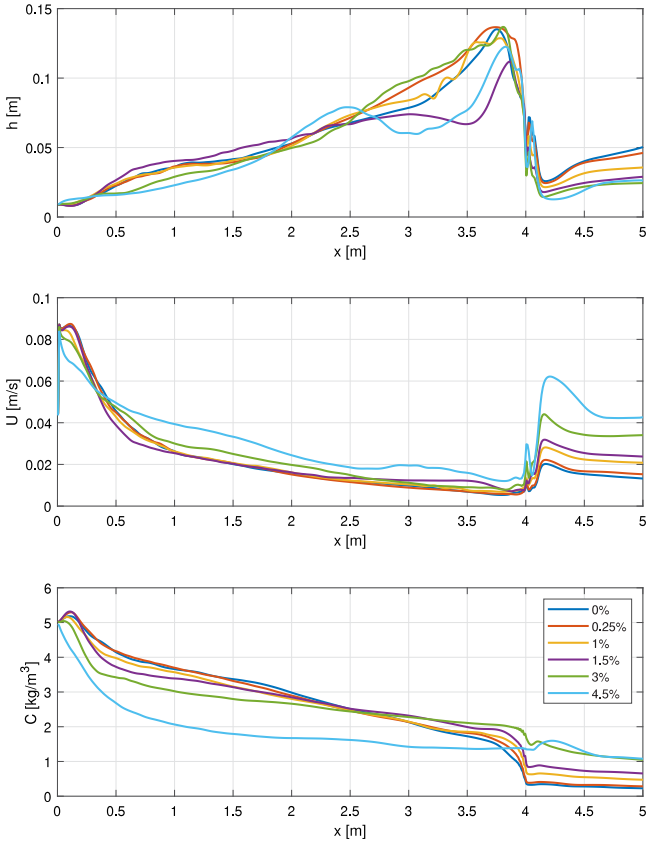

Fig. 11. Streamwise evolution of the turbidity current characterizing parameters during the quasi-stead state.

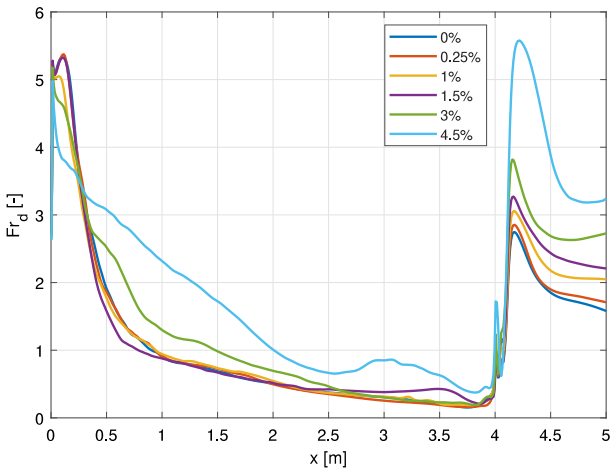

Fig. 12. Local densimetric Froude number at the quasi-steady state based on the middle 30 cm of the channel width.

The densimetric Froude number in the bore's frame $F_{rd,b}$ can be calculated using the following relationship:

$$F_{rd,b} = \frac{U - U_b}{\sqrt{\Delta g C_v h \cos\theta}}, \tag{15}$$

where U_b is the bore propagation velocity (negative for backward motion).

We calculated $F_{rd,b}$ for three cases — 0.25%, 1.5%, and 4.5% bed slopes — at $T = 241$ seconds, yielding values of 0.54, 0.47 and 0.22, respectively. These results are consistent with the findings of Huang et al. (2009), who reported that the critical densimetric Froude number of subaqueous gravity currents can deviate from unity.

4.6. Sediment transport and deposition

The suspended sediment flux per unit width $\dot{m}$ [kg/m/s] can be calculated by:

$$\dot{m} = \int_0^{z_\infty} uc \, \mathrm{d}z. \tag{16}$$

The dimensionless net deposition rate is defined as:

$$R = \frac{\dot{m}_{in} - \dot{m}}{\dot{m}_{in}}. \tag{17}$$

where $\dot{m}_{in}$ is the inlet suspended sediment flux per unit width.

The influence of bed slope on suspended sediment transport and deposition in the quasi-steady state is illustrated in Fig. 13. In general, the suspended sediment flux decreases progressively along the flume, with the highest reduction observed for the horizontal bed and the least for the steepest slope considered (Fig. 13, left panel). Upstream the obstacle, the greater sediment flux associated with steeper slopes primarily results from higher flow velocities rather than increased sediment concentrations (see Section 4.3). The sediment flux on the top of obstacle (at $x = 4$ m) increases with the bed slope. Downstream from the flume inlet, the rate of sediment deposition increases, exhibiting the highest value ($R = 0.93$) for the horizontal bed and the lowest ($R = 0.40$) for the steepest bed slope at $x = 5$ m. In conclusion, steeper bed slopes enhance the sediment transport capacity of the flow predominantly through increased flow velocity, resulting in reduced sediment deposition rates along the sloping bed.

These results highlight the role of bed slope in controlling sediment retention efficiency upstream of the obstacle. Milder slopes promote increased sediment deposition and retention, whereas steeper slopes favor sediment bypass due to higher flow velocities and transport capacity. In artificial environments such as reservoirs, this behavior directly affects the effectiveness of obstacles in retaining sediment and protecting downstream infrastructure, while in natural settings it provides insight into how slope and seabed topography govern sediment bypass and accumulation in turbidity current systems.

4.7. Limitations

It is worth highlighting some limitations of this study. First, the range of bed slopes investigated is limited to relatively gentle gradients (0–4.5%), which are representative of many reservoir settings but do not encompass the steeper slopes (> 5%) commonly observed in submarine canyons. Second, the analysis focuses primarily on quasi-steady-state flow conditions upstream of the obstacle, with less emphasis on transient flow behavior. While this approach allows a systematic comparison of slope effects, it does not capture short-term unsteady processes that may influence sediment transport. Third, the simulations are conducted in a confined channel with simplified geometry and constant bed slope. In natural and engineered environments, more complex topography may modify flow structure, recirculation patterns, and sediment distribution. Finally, the relatively small inlet flow rate resulted in flow velocities that were insufficient to entrain sediment from the bed. In reality, bed erosion and deposition would alter local topography, leading to morphodynamic feedback processes. These limitations provide context for the present findings and highlight directions for future research.

5. Conclusion

In this study, three-dimensional numerical simulations based on the Large Eddy Simulation (LES) technique were conducted to examine the

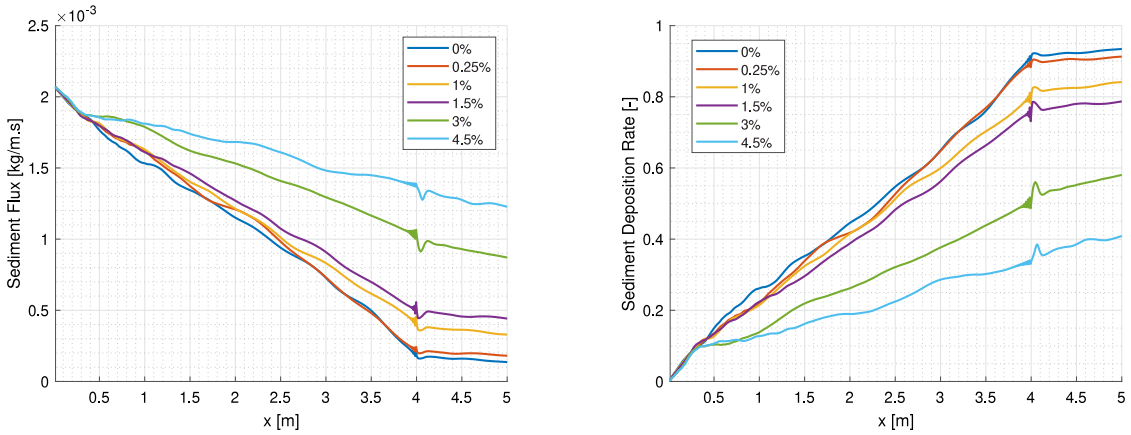

Fig. 13. Suspended sediment Flux (left) and deposition rate (right).

influence of bed slope on the dynamics and depositional behavior of turbidity currents interacting with a triangular obstacle. The analysis focused mostly on the quasi-steady-state flow conditions upstream of the obstacle. A strong dependence of the sediment-retention efficiency on bed slope was revealed. Specifically, at steeper slopes, a larger portion of sediment particles passes over the obstacle. Besides, steeper slopes promote higher flow velocities and enhanced sediment transport capacity, leading to reduced sediment deposition rates along the bed and thus a decline in the obstacle's sediment-retention performance. For the milder bed slopes (0–1.5%), the bore generated by the obstacle propagates upstream and reaches the inlet boundary, indicating that the obstacle influences the sediment flux throughout the entire upstream region. Furthermore, the local densimetric Froude number analysis showed a distinct transition in flow regime across the obstacle. The current exhibited negligible velocity upstream, indicating a subcritical state; however, upon passing over the obstacle, the velocity increased sharply, transitioning the flow to a supercritical regime.

Overall, the findings provide valuable insights into the complex interactions between turbidity currents, bed slope, and an obstacle. While the results are directly relevant for sediment management and engineering design in reservoirs and hydraulic structures, they also have broader implications for natural submarine environments, contributing to a better understanding of sedimentary processes in both engineered and natural systems.

CRediT authorship contribution statement

Said Alhaddad: Writing – review & editing, Writing – original draft, Visualization, Validation, Supervision, Resources, Project administration, Methodology, Investigation, Formal analysis, Data curation, Conceptualization. **Ching-Sen Wu:** Writing – review & editing, Conceptualization. **Lynyrd de Wit:** Writing – review & editing, Software, Methodology, Conceptualization.

Declaration of competing interest

The authors declare that they have no known competing financial interests or personal relationships that could have appeared to influence the work reported in this paper.

Data availability

The source code of the numerical model used in this study is publicly available at https://github.com/openearth/tudflow3d.

References

Abhari, M.N., Iranshahi, M., Ghodsian, M., Firoozabadi, B., 2018. Experimental study of obstacle effect on sediment transport of turbidity currents. J. Hydraul. Res. 56 (5), 618–629.

Alexander, J., Morris, S., 1994. Observations on experimental, nonchannelized, high-concentration turbidity currents and variations in deposits around obstacles. J. Sediment. Res. 64 (4a), 899–909.

Alhaddad, S., de Wit, L., Labeur, R.J., Uijttewaal, W., 2020a. Modeling of breaching-generated turbidity currents using large eddy simulation. J. Mar. Sci. Eng. 8 (9), 728.

Alhaddad, S., Keetels, G., Mastbergen, D., van Rhee, C., Lee, C.-H., Montellà, E.P., Chauchat, J., 2024a. Subaqueous dilative slope failure (breaching): Current understanding and future prospects. Adv. Water Resour. 104708.

Alhaddad, S., Labeur, R.J., Uijttewaal, W., 2020b. Large-scale experiments on breaching flow slides and the associated turbidity current. J. Geophys. Res.: Earth Surf. 125 (10), e2020JF005582.

Alhaddad, S., Suleman, M., Kirichek, A., Chassagne, C., 2024b. Experimental investigation of cohesive soil erosion and suspension caused by a coandă-effect-based polymetallic-nodule collector. Results Eng. 22, 102231.

Biegert, E., Vowinckel, B., Ouillon, R., Meiburg, E., 2017. High-resolution simulations of turbidity currents. Prog. Earth Planet. Sci. 4 (1), 33.

Bourget, J., Zaragosi, S., Ellouz-Zimmermann, S., Ducassou, E., Prins, M., Garlan, T., Lanfumey, V., Schneider, J.-L., Rouillard, P., Giraudeau, J., 2010. Highstand vs. lowstand turbidite system growth in the makran active margin: Imprints of high-frequency external controls on sediment delivery mechanisms to deep water systems. Mar. Geol. 274 (1–4), 187–208.

Cerqueira, A.C., Manica, R., 2022. Effects caused by obstacles in the hydrodynamics of turbidity currents: an experimental approach. RBRH 27, e20.

Cesare, G.D., Schleiss, A., Hermann, F., 2001. Impact of turbidity currents on reservoir sedimentation. J. Hydraul. Eng. 127 (1), 6–16.

Chamoun, S., De Cesare, G., Schleiss, A.J., 2017. Management of turbidity current venting in reservoirs under different bed slopes. J. Environ. Manag. 204, 519–530.

Choi, S.-U., García, M.H., 2002. K-ϵ turbulence modeling of density currents developing two dimensionally on a slope. J. Hydraul. Eng. 128 (1), 55–63.

de Wit, L., 2015. 3D CFD Modelling of Overflow Dredging Plumes (Ph.D. thesis). Delft University of Technology.

de Wit, L., van Rhee, C., 2014. Testing an improved artificial viscosity advection scheme to minimise wiggles in large eddy simulation of buoyant jet in crossflow. Flow, Turbul. Combust. 92 (3), 699–730.

Dodd, M.S., Ferrante, A., 2014. A fast pressure-correction method for incompressible two-fluid flows. J. Comput. Phys. 273, 416–434.

Dorrell, R., Peakall, J., Sumner, E., Parsons, D., Darby, S., Wynn, R., Özsoy, E., Tezcan, D., 2016. Flow dynamics and mixing processes in hydraulic jump arrays: Implications for channel-lobe transition zones. Mar. Geol. 381, 181–193.

Fadlun, E.A., Verzicco, R., Orlandi, P., Mohd-Yusof, J., 2000. Combined immersed-boundary finite-difference methods for three-dimensional complex flow simulations. J. Comput. Phys. 161 (1), 35–60.

Farizan, A., Yaghoubi, S., Firoozabadi, B., Afshin, H., 2019. Effect of an obstacle on the depositional behaviour of turbidity currents. J. Hydraul. Res. 57 (1), 75–89.

Gonzalez-Juez, E., Meiburg, E., Constantinescu, G., 2009. Gravity currents impinging on bottom-mounted square cylinders: flow fields and associated forces. J. Fluid Mech. 631, 65–102.

Goodarzi, D., Sookhak Lari, K., Khavasi, E., Abolfathi, S., 2020. Large eddy simulation of turbidity currents in a narrow channel with different obstacle configurations. Sci. Rep. 10 (1), 12814.

Huang, H., Imran, J., Pirmez, C., Zhang, Q., Chen, G., 2009. The critical densimetric froude number of subaqueous gravity currents can be non-unity or non-existent. J. Sediment. Res. 79 (7), 479–485.

Kirichek, A., Cronin, K., de Wit, L., van Kessel, T., 2021. Advances in maintenance of ports and waterways: Water injection dredging. In: Manning, A.J. (Ed.), Sediment Transport - Recent Advances. IntechOpen, London.

Kneller, B., Buckee, C., 2000. The structure and fluid mechanics of turbidity currents: a review of some recent studies and their geological implications. Sedimentology 47, 62–94.

Mahgoub, M., Keetels, G., Alhaddad, S., 2025. Impact of operational parameters on turbidity generation in cutter suction dredging: Insights from a numerical model and sensitivity analysis. Appl. Ocean Res. 154, 104312.

Manninen, M., Taivassalo, V., Kallio, S., 1996. On the Mixture Model for Multiphase Flow VTT Publications 288. Technical Research Center of Finland.

Morris, S.A., Alexander, J., 2003. Changes in flow direction at a point caused by obstacles during passage of a density current. J. Sediment. Res. 73 (4), 621–629.

Nasr-Azadani, M.M., Meiburg, E., 2014. Influence of seafloor topography on the depositional behavior of bi-disperse turbidity currents: a three-dimensional, depth-resolved numerical investigation. Environ. Fluid Mech. 14 (2), 319–342.

Nicoud, F., Ducros, F., 1999. Subgrid-scale stress modelling based on the square of the velocity gradient tensor. Flow, Turbul. Combust. 62 (3), 183–200.

Oehy, C.D., Schleiss, A.J., 2007. Control of turbidity currents in reservoirs by solid and permeable obstacles. J. Hydraul. Eng. 133 (6), 637–648.

Parker, G., García, M., Fukushima, Y., Yu, W., 1987. Experiments on turbidity currents over an erodible bed. J. Hydraul. Res. 25 (1), 123–147.

Parsons, J.D., Bush, J.W., Syvitski, J.P., 2001. Hyperpycnal plume formation from riverine outflows with small sediment concentrations. Sedimentology 48 (2), 465–478.

Prosperetti, A., Tryggvason, G., 2007. Computational Methods for Multiphase Flow. Cambridge University Press.

Talling, P.J., Allin, J., Armitage, D.A., Arnott, R.W., Cartigny, M.J., Clare, M.A., Felletti, F., Covault, J.A., Girardclos, S., Hansen, E., et al., 2015. Key future directions for research on turbidity currents and their deposits. J. Sediment. Res. 85 (2), 153–169.

Woods, A.W., Bursik, M.I., Kurbatov, A.V., 1998. The interaction of ash flows with ridges. Bull. Volcanol. 60 (1), 38–51.

Yaghoubi, S., Afshin, H., Firoozabadi, B., Farizan, A., 2017. Experimental investigation of the effect of inlet concentration on the behavior of turbidity currents in the presence of two consecutive obstacles. J. Waterw. Port, Coast. Ocean. Eng. 143 (2), 04016018.

Yeh, T.-h., Cantero, M., Cantelli, A., Pirmez, C., Parker, G., 2013. Turbidity current with a roof: Success and failure of RANS modeling for turbidity currents under strongly stratified conditions. J. Geophys. Res.: Earth Surf. 118 (3), 1975–1998.